ACS OMEGA

http://pubs.acs.org/journal/acsodf

Article

Microwave-Assisted Auto-Combustion Synthesis of Binary/Ternary Co_xNi_{1-x}Ferrite for Electrochemical Hydrogen and Oxygen Evolution

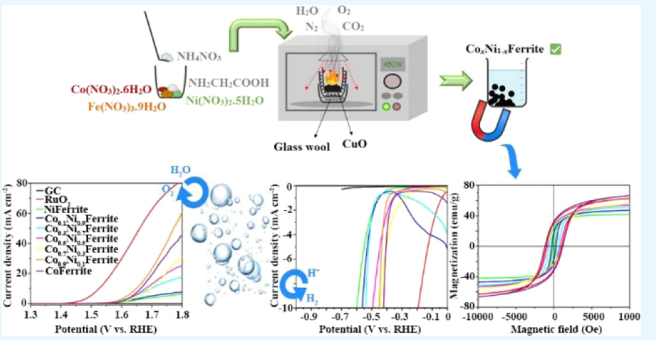
Sanaz Chamani, Maasoumeh Khatamian,* Naeimeh Sadat Peighambardoust, and Umut Aydemir*

Cite This: *ACS Omega* 2021, 6, 33024−33032

Read Online

ACCESS | Metrics & More | Article Recommendations | Supporting Information

ABSTRACT: Enormous efforts have been dedicated to engineering low-cost and efficient electrocatalysts for both hydrogen evolution and oxygen evolution reactions (HER and OER, respectively). For this, the current contribution reports the successful synthesis of binary/ternary metal ferrites (Co_xNi_{1-x}Ferrite; x = 0.0, 0.1, 0.3, 0.5, 0.7, and 1.0) by a simple one-step microwave technique and subsequently discusses its chemical and electrochemical properties. The X-ray diffraction analysis substantiated the phase purity of the as-obtained catalysts with various compositions. Additionally, the morphology of the nanoparticles was identified via transmission electron microscopy. Further, the vibrating sample magnetometer justified the ferromagnetic character of the as-prepared products. The electrochemical measurements revealed that the as-prepared materials required the overpotentials of 422−600 and 419−467 mV for HER and OER, respectively, to afford current densities of 10 mA cm^{-2}. In the general sense, Ni cation substitution with Co influenced favorably toward both HER and OER. Among all synthesized electrocatalysts, $Co_{0.9}Ni_{0.1}$Ferrite displayed the highest performance in terms of OER in 1 M KOH solution, which is related to the synergistic effect of multiple parameters including the optimal substitution amount of Co, the highest Brunauer−Emmett−Teller surface area, the smallest particle size among all samples (26.71 nm), and the lowest charge transfer resistance. The successful synthesis of ternary ferrites carried out for the first time via a microwave-assisted auto-combustion route opens up a new path for their applications in renewable energy technologies.



Downloaded via KOC UNIV on February 13, 2022 at 18:55:37 (UTC).
See https://pubs.acs.org/sharingguidelines for options on how to legitimately share published articles.

1. INTRODUCTION

The huge consumption of unsustainable carbon-emitting fossil fuels is the primary culprit for the current energy crunch and environmental concerns.[1,2] Hydrogen, a carbon-free energy source is a favorable response to confront the energy crisis and environmental issues such as global warming.[3,4] Discovering a completely new, environmentally benign, cheap, and efficacious strategy to generate hydrogen is a persistent challenge. Electrochemical water splitting stands out among other systems regarding its benefits including hydrogen production with high purity and leaving no carbon footprints.[5−7] This process consists of two half-reactions, namely, hydrogen evolution reaction (HER) on the cathode and oxygen evolution reaction (OER) on the anode.[6,8] So far, precious-metal-based electrocatalysts such as Pt/C and RuO_2 have been identified as state-of-the-art materials to drive the reaction and lower the overpotential higher than the theoretical one, 1.23 V.[9,10]

Over the past decades, plenty of attempts have been made to design and develop catalysts that alloys,[11−13] carbides,[14,15] nitrides,[16,17] oxides,[18−20] phosphides,[21−23] borides,[24,25] and chalcogenides[26,27] are some of the materials that have been widely explored. Amidst a wide spectrum of electrocatalytic chemicals, the well-known metal compounds of Fe, Co, and Ni—located in the same group with Ru, Ir, and Pt, individually and hence expected to show relatively identical catalytic traits[5]—and different compositions of their mixed oxides are believed to have outstanding catalytic activity for electrolysis of water.[28,29] It is generally presumed that multinary mixed oxides should outperform their unary counterparts by the virtue of their intrinsic merits such as desirable electrical and catalytic abilities.[30−34] Keeping this in mind, to accurately evaluate the performance of these oxides, their compositions and particularly content of metal ions should be taken into consideration.[34]

To narrow down the list of mixed metal oxides, some can hold a high potential for energy conversion and storage.[31−33,35] For instance, $NiCo_2O_4$[36,37] Ni−Fe mixed oxide,[38] and (Fe, Co, Ni, and Mn) oxides[39,40] are favorable electrocatalysts for HER and/or OER. To this end, magnetic ferrites with a general

Received: September 18, 2021
Accepted: November 10, 2021
Published: November 22, 2021



© 2021 The Authors. Published by American Chemical Society

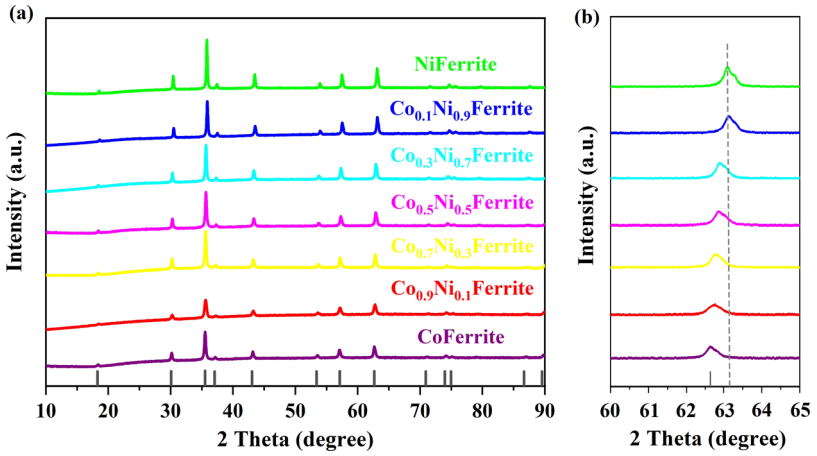


Figure 1. (a,b) XRD patterns of the prepared Co_xNi_{1-x}Ferrite samples.

formula of MFe_2O_4 (M = Ni, Co, Cu, Mn, and so on) are a critical family of mixed metal oxides with innate benefits such as tunable redox properties, high abundance, and inexpensiveness[35] have attracted a great deal of research interest. The so-called nano-structured spinel ferrite represents a cubic, close packing configuration of oxygen atoms, in which M^{2+} (M = Co, Ni) and Fe^{3+} ions can fill tetrahedral or octahedral interstitial sites.[41,42] Spinel ferrites have diverse applications in multi-disciplinary areas but are not limited to high-density magnetic recording, magnetic fluids, sensors, and catalysis to name but a few.[43,44]

Thus far, multiple approaches have been adopted for the synthesis of nano-structured ferrites including but not limited to sol−gel, hydrothermal, solvothermal, high-energy ball milling, chemical co-precipitation, and citric acid combustion.[45−48] Nonetheless, costly and complicated processes along with low production rates are the typical flaws from which these methods suffer.[45] Amidst the documented techniques, microwave combustion synthesis has gained extensive research interest. High rates of reaction, shorter reaction time, less energy usage, high yield, and quality of resulting products are some of the merits of the microwave combustion method as opposed to other synthetic routes.[45−48]

We present herein the synthesis of binary/ternary metal ferrites [Co_xNi_{1-x}Ferrite (x = 0.0, 0.1, 0.3, 0.5, 0.7, and 1.0)] by the aid of auto-combustion approach using microwave for the first time. The as-prepared materials were explored for their magnetic, chemical, and electrochemical properties. The results disclosed that increasing Co concentration, in general, has a positive impact on both HER and OER performance.

2. RESULTS AND DISCUSSION

2.1. Characterization. The X-ray diffractometer (XRD) was employed to verify the structural phase purity and determine the crystallite size of the prepared spinel nanoparticles. Figure 1a depicts the reflected characteristic peaks of the Co_xNi_{1-x}Ferrites nanoparticles. The appeared XRD peaks at 2θ about 18.41, 30.29, 35.68, 37.33, 43.37, 53.82, 57.37, 63.1, and 74.57 can be indexed to the (111), (220), (311), (222), (400), (422), (511), (440), and (533) planes, separately, which confirmed the presence of a single-phase cubic spinel structure without secondary phases matched very well with the JCPDS card no. 74-2081 for $NiFe_2O_4$ and JCPDS card no. 77-0426 for $CoFe_2O_4$, respectively. To calculate the average particle size the Scherrer's equation was exploited according to the following relation

$$D = k\lambda/\beta \cos\theta$$

where D denotes the average particle size, k = 0.89 is the shape factor of a particle, λ = 1.5406 Å is the X-ray wavelength used, β is the full width at half-maximum of the XRD (311) peak, and θ is Bragg's angle in degrees unit. The average particle size of the magnetic nanoparticles was estimated in the range of 26−43 nm (refer to Table S1). It should be pointed out that dashed line around 2θ of 63.1 from top to the bottom by increasing Co quantity, peak shifts to smaller 2θ which is an indication of Co substitution in the structure of NiFerrite, and therefore larger lattice parameters (see Figure 1b).

The construction of Co_xNi_{1-x}Ferrite nanoparticles was substantiated by Fourier transform infrared characterization (FT-IR). In accordance with Figure 2, no secondary

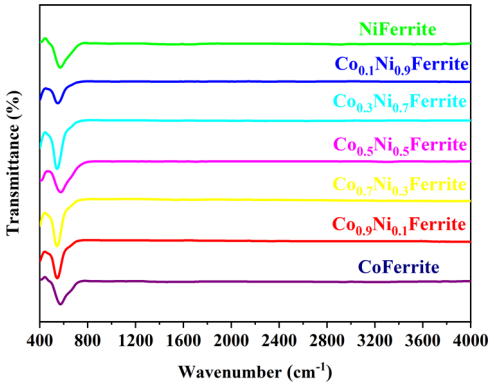


Figure 2. FT-IR spectrum of synthesized Co_xNi_{1-x}Ferrite samples.

absorption bands regarding organic groups were detected above 1000 cm^{-1}. The two metal−oxygen (M−O) absorption bands observed in the range of 400−600 cm^{-1} can be attributed to the vibration of ions in the crystal lattices. The presence of maximum bands within the 500−600 cm^{-1} corresponds to cardinal stretching vibrations of the metal at the tetrahedral site, whereas the bands usually witnessed under 450 cm^{-1}, are indexed to the octahedral metal stretching site.

To inspect the surface morphology and chemical composition of the ferrite powders. Scanning electron microscopy (SEM) coupled with energy dispersive X-ray spectroscopy

https://doi.org/10.1021/acsomega.1c05183
ACS Omega 2021, 6, 33024−33032

(EDS) elemental analyses were conducted. Figure 3a–c exhibits the dense agglomeration of nanoparticles for both

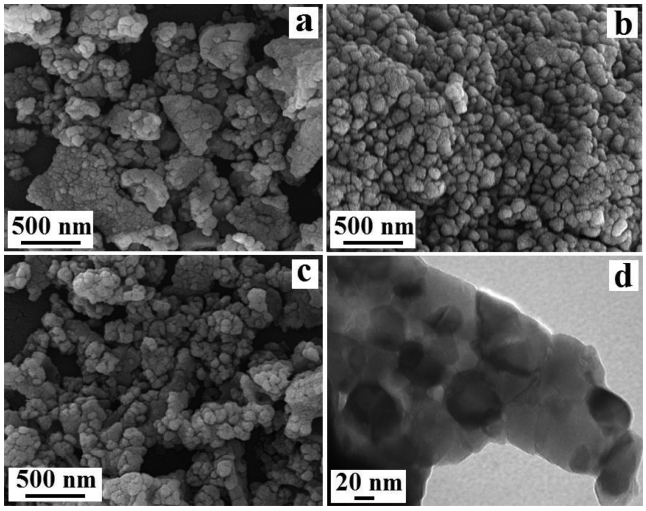


Figure 3. SEM images of (a) NiFerrite, (b) CoFerrite, (c) $Co_{0.9}Ni_{0.1}$Ferrite, and (d) TEM of $Co_{0.9}Ni_{0.1}$Ferrite nanoparticles.

doped and undoped samples which can be attributed to the magnetic properties of the synthesized materials (SEM images of remaining materials are included in Figure S1). Even though the accurate shape of particles cannot be evidenced, the transmission electron microscopy (TEM) image shown in Figure 3d manifests the cubic shape of the particles. It should be noted that further data regarding the elemental studies of the samples can be observed in Supporting Information, Figure S2, and Table S2. The high-resolution TEM (HRTEM) images of $Co_{0.9}Ni_{0.1}$Ferrite (Figure 4) shows the lattice fringes with a lattice spacing of 0.496 nm, corresponding to the (111) of CoFerrite.

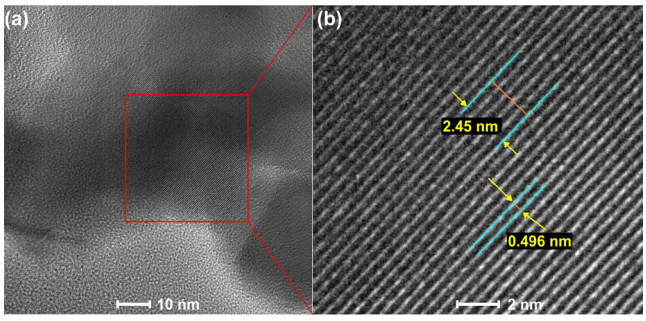


Figure 4. (a,b) HRTEM images of $Co_{0.9}Ni_{0.1}$Ferrite.

The magnetic properties of Co_xNi_{1-x}Ferrite nanoparticles were achieved through a vibrating sample magnetometer at room temperature. A very clear hysteresis loop was exhibited (Figure 5) from the *M*–*H* measurements, which proves the ferromagnetic nature of magnetic ferrite nanoparticles. Multiple magnetic features can be achieved via the hysteresis loops including saturation magnetization (Ms), coercivity (Hc), and remanence magnetization (Mr), and the observed values are summarized in Table 1. It was observed that the highest Ms value and coercivities (Hc) for CoFerrite is 66.4 emu/g and 1174.5 Oe. The result manifests that Ms and Hc of the samples are in direct correlation with Co content. The magnetic

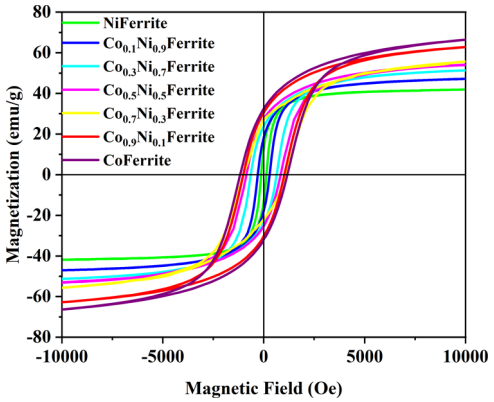


Figure 5. Magnetization curve of the magnetic nanoparticles.

Table 1. Variation of Ms, Hc, and Mr of Spinel Co_xNi_{1-x}Ferrite Nanoparticles

sample	Ms	Hc	Mr
NiFerrite	41.5	−129.6	13
$Co_{0.1}Ni_{0.9}$Ferrite	47.2	−294.2	18.2
$Co_{0.3}Ni_{0.7}$Ferrite	51.3	−639.7	23.8
$Co_{0.5}Ni_{0.5}$Ferrite	55	−863.7	27
$Co_{0.7}Ni_{0.3}$Ferrite	55.7	−1004.8	27
$Co_{0.9}Ni_{0.1}$Ferrite	62.8	−1019.9	30.5
CoFerrite	66.4	−1174.5	32.5

moments of $Ni^{2+}$and Co^{2+} are 2.82 μ_B and 3.87 μ_B (Bohr magneton), respectively. Therefore, proliferation in the number of Ni^{2+}sites replaced by Co^{2+}brings about larger Ms and Mr (remanence) values. On the contrary, Hc values of ferrites grow bigger as a result of the larger ion radius of Co^{2+} (0.78 A) as opposed to Ni^{2+} (0.7 Å), giving rise to the lattice expansion (refer to Figure 1b). Thus, the widening of both interplanar spatial spacings of the particles impedes the response of particles to the external magnetic field.

2.2. Electrochemical Studies. The electrochemical properties of prepared catalysts for HER and OER were evaluated on GC = with 0.125 mg cm^{-2} catalyst loading as a working electrode in 1 M KOH solution. Figure 6a demonstrates the linear sweep voltammetry (LSV) polarization curves of electrocatalysts toward HER inclusive of GC and 10% Pt/C. As it can be seen, GC shows insignificant electrochemical activity, verifying its inertness. On the contrary, 10% Pt/C reveals a low onset potential of 198 mV to achieve 10 mA cm^{-2}. The overpotential values of the as-synthesized samples are tabulated in Table 2. A glance at this table discloses the fact that NiFerrite suffers from low performance (600 mV at 10 mA cm^{-2}), whereas CoFerrite enjoys the highest performance (422 mV at 10 mA cm^{-2}) relative to other samples. Not to mention that HER performance and Co concentration are roughly in direct relation, suggesting that increasing Co content leads to a positive effect on HER activity. In fact, the Co element is believed to be a favorable factor in improving HER due to its moderate H-bonding energy. Incorporation of trace amount of Co into the lattice of catalysts can substantially alter the electronic structure.[49−51] The earlier studies manifested that the catalytic performance is strongly dependent on the Co doping levels, and thus only a proper concentration of Co can boost the inherent conductivity and decline the adsorption energy of H atoms (ΔG_{H^*}). For an instance, for Co-doped

https://doi.org/10.1021/acsomega.1c05183
ACS Omega 2021, 6, 33024−33032

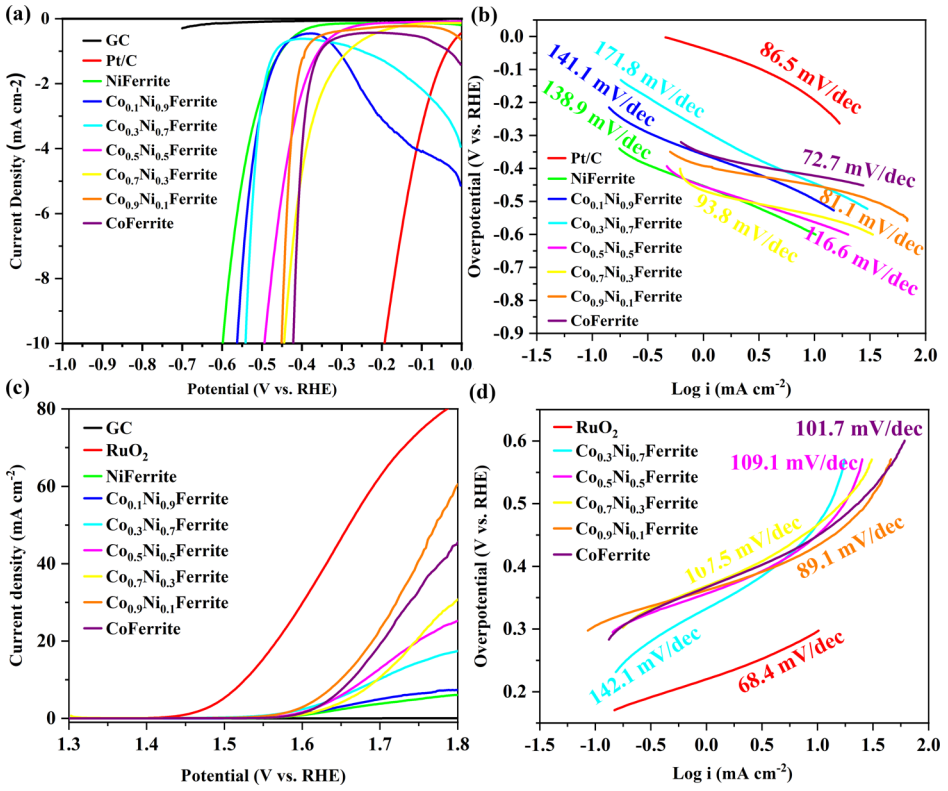


Figure 6. Electrochemical studies of Co_xNi_{1-x}Ferrite nanoparticles. (a) Polarization curves toward HER and (b) corresponding Tafel plots. (c) Polarization curves toward OER and (d) corresponding Tafel plots.

Table 2. Overpotential Values of As-prepared Catalysts for HER and OER in 1 M KOH Medium and Corresponding Brunauer–Emmett–Teller (BET) Surface Area

sample	HER overpotential (mV)	OER overpotential (mV)	BET surface area (m^2/g)
Pt/C	198		
RuO_2		290	
NiFerrite	600		4.66
$Co_{0.1}Ni_{0.9}$Ferrite	566		7.08
$Co_{0.3}Ni_{0.7}$Ferrite	541	467	5.88
$Co_{0.5}Ni_{0.5}$Ferrite	495	451	7.12
$Co_{0.7}Ni_{0.3}$Ferrite	446	467	9.45
$Co_{0.9}Ni_{0.1}$Ferrite	451	419	12.10
CoFerrite	422	434	11.35

FeS_2 nanosheets, it was found that a Co/Fe ratio of 1:9 resulted in the highest HER activity. The density functional theory calculations revealed that the Co doping greatly decreased the energy barrier of H adsorption on the FeS_2 surface. Considering the points mentioned above, the same scenario can be developed for the present work—in that—adsorption energy of H atoms on the surface has gradually decreased with increasing Co concentration, giving rise to the best HER performance for the case of CoFerrite.[50,52]

Catalysts based on earth-abundant Co have received tremendous research interest owing to their intrinsic electrocatalytic capacity toward HER and/or OER.[53−56] Previous studies have validated that spinels of cobalt can contribute to higher electronic conductivity as well as the number of active sites, which in turn reflect in greater electrochemical features.[57] Previously, it has been proven that the electronic structure of a catalyst can be modulated and thereby promoted by the incorporation of more cations. Comparing bimetallic spinels of Co and Ni in this work, we can notice the positive impact of cation introduction in both cases of HER and OER. Compared to HER, NiFerrite still holds inferior performance for OER. However, $Co_{0.9}Ni_{0.1}$Ferrite is the best performing catalyst (419 mV at 10 mA cm^{-2}), exceeding the performance of CoFerrite (434 mV at 10 mA cm^{-2}), thanks to optimized charge transfer between bimetals of Co and Ni (Figure 6c). In many cases, the incorporation of more metal atoms can modify the adsorption energy of reaction intermediates and improve catalytic activity.[58,59] In addition, according to the calculated particle size in Table S1, the smallest size corresponds to $Co_{0.9}Ni_{0.1}$Ferrite (26.71 nm), a beneficial contribution to OER electrocatalytic activity.[34] It should be pointed out that benchmark RuO_2 was also evaluated toward OER, implying that as-synthesized catalysts are less efficient, yet fairly promising regarding their economic precursors, green fabrication method, and easily scalable procedure.

In principle, Co-containing ferrites are preferably viewed as favorable electrocatalysts toward OER,[34,60,61] in which their activities can be altered by size, morphology,[62] and hybrid forming.[63,64] The surface of Co-bearing catalysts under alkaline conditions transforms to thermodynamically stable species such as Co-(oxy) hydroxide (CoOOH) which can function as active sites for the oxygen-evolving reaction.[2] It is believed that the OER mechanism is subject to the occurrence of four successive steps.

$$\text{Step 1: } Co^{II} + 3OH^- \leftrightarrow Co^{III}OOH + H_2O(l) + e^-$$

$$\text{Step 2: } Co^{III}OOH + OH^- \leftrightarrow Co^{IV}O(OH)_2 + e^-$$

https://doi.org/10.1021/acsomega.1c05183
ACS Omega 2021, 6, 33024−33032

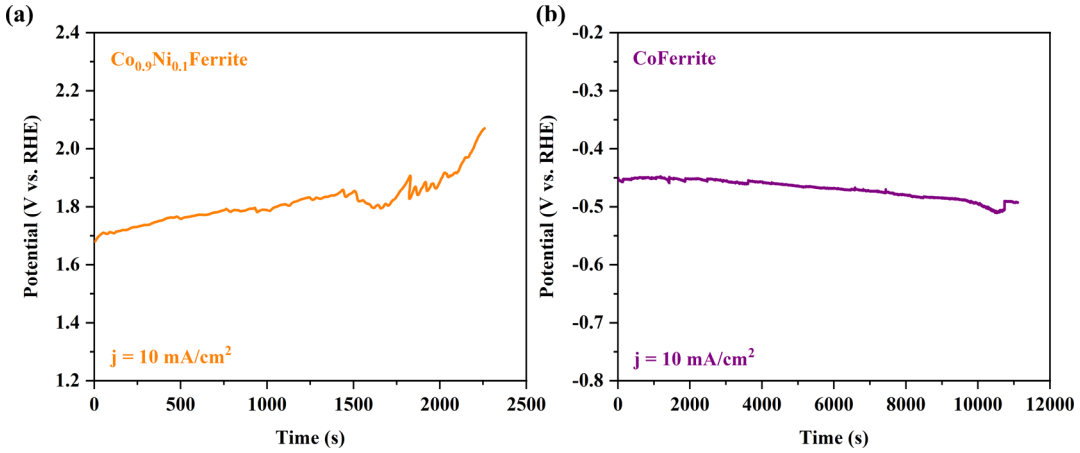


Figure 7. Chronopotentiometric curves recorded at a current density of 10 mA cm^{-2} of the best-performing catalysts.

Step 3: $Co^{IV}O(OH)2 + 2OH^-$

$\leftrightarrow Co^{IV}OO_2 + 2H_2O(l) + 2e^-$

Step 4: $Co^{IV}OO_2 + OH^- \leftrightarrow Co^{III}OOH + O_2(g) + e^-$

From a thermodynamic point of view, the last step is irreversible ($\Delta G_4 < 0$). Thus, one of three remaining reversible steps is the rate-controlling step. During OER, $Co^{II}/Co^{III}/Co^{IV}$ mixed states are the dominating cobalt species. Here, $Co^{III}OOH$, $CoO^{IV}(OH)_2$, and $Co^{IV}OO_2$ represent the adsorbed intermediates on the surface-active sites, and (l) and (g) denote liquid and gas phases, individually. Concerning the investigated samples and particularly the best-performing one, $Co_{0.9}Ni_{0.1}$Ferrite, the catalyst goes under partial oxidation, converting to $Co^{III}OOH$ followed by an electron release (step 1). Nest, $Co^{III}OOH$ reacts with another OH^-, producing $Co^{IV}O(OH)_2$and an electron (step 2). Afterward, $Co^{IV}O(OH)_2$ reacts with two other OH^-, generating $Co^{IV}OO_2$, two water molecules, and two electrons (Step 3). Finally, $Co^{IV}OO_2$ combines with another OH^- to form O_2 gas, a $Co^{III}OOH$, and an electron (Step 4). As a whole, mixed cobalt states on the catalyst surface create more active sites and hence encourage the charge transfer.[53,65,66]

From Figure 6b, calculated Tafel slopes can be seen. The Tafel slope is a key indicator to ascertain the HER kinetics, establishing the rate-controlling step during the reaction.[24,67] The two general routes reported in the literature[68−70] for hydrogen evolution under basic conditions are as follows

a) $H_2O(1) + e^- + ^\circ \rightarrow H^\circ + OH^-(aq)$, Volmer reaction

b) $H^\circ + H_2O(1) + e^- \rightarrow H_2(g) + OH^-(aq) + ^\circ$, Heyrovsky reaction

c) $H_2O(1) + e^- + ^\circ \rightarrow H^\circ + OH^-(aq)$, Volmer reaction

d) $H^\circ + H^\circ \rightarrow H_2(g) + 2^\circ$, Tafel reaction

Therefore, the adsorption−desorption process either takes place via the Volmer−Heyrovsky mechanism (a,b) or the Volmer−Tafel mechanism (c,d). Here, ° and H° stand for available active sites and hydrogen atoms adsorbed on the active sites, respectively. The estimated Tafel slopes for the Volmer reaction, Heyrovsky reaction, and Tafel reaction are respective values of ∼120 mV dec^{-1}, ∼40 mV dec^{-1}, and ∼30 mV dec^{-1},[68] The results exhibit that commercial 10% Pt/C as a reference material has a slope of 86.5 mV dec^{-1} which is in the region of 40−120 mV dec^{-1}, suggesting the Volmer−Heyrovsky mechanism. Among the prepared samples, CoFerrite and $Co_{0.9}Ni_{0.1}$Ferrite display the smallest Tafel slopes (72.7 mV dec^{-1} and 81.1 mV dec^{-1}) compared to other catalysts and reference material, suggesting the Volmer−Heyrovsky path. The corresponding Tafel plots for OER are shown in Figure 6d. According to this figure, RuO_2 owns the smallest Tafel slope (68.4 mV dec^{-1}) and hence enjoys the fastest kinetics. Amidst the as-synthesized electrocatalysts, $Co_{0.9}Ni_{0.1}$Ferrite holds the lowest slope value (89.1 mV dec^{-1}), which is in line with its OER performance. The preceding statements accord with the BET results, meaning that the sample endowing with the highest BET surface area enjoys the best OER activity (Table 2). It should be noted that the comparison of present results with those of previously reported spinel catalysts in OER and HER has been tabulated in Table S3.

Because catalytic sustainability has a central role in water splitting applications, the longevity of the best-performing catalysts in OER ($Co_{0.9}Ni_{0.1}$Ferrite) and HER (CoFerrite) were also measured and recorded at a current density of 10 mA cm^{-2} (Figure 7). Moreover, the microstructure of these materials after electrochemical operations was studied (see Figure S3). According to the SEM images, no pronounced alteration was detected after OER and HER experiments on the surface of electrodes in terms of morphology. In addition, the EDS elemental analyses confirmed the presence of initial elements in the matrices of as-obtained electrocatalysts.

The electrochemical impedance spectroscopy (EIS) experiments were performed to inspect the charge transfer resistance. Figure 8 presents the Nyquist plots along with equivalent circuits once the samples were placed in contact with electrolyte. Re indicates the resistance of the solution between the working and reference electrodes. CPE and Rct stand for the impedances of the interfacial reactions on the surface, namely, capacitive component and Faraday resistance, individually. Finally, Warburg impedance (W) was added to the equivalent circuit, indicating that diffusion is the controlling step on the surface.

https://doi.org/10.1021/acsomega.1c05183
ACS Omega 2021, 6, 33024−33032

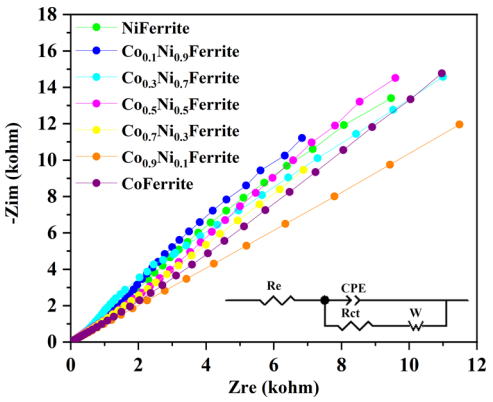


Figure 8. Nyquist plots of Co_xNi_{1-x}Ferrite nanoparticles.

Table 3 summarizes the calculated values of the equivalent circuit parameters using ZView software. The results exhibit two types of behavior based on the cobalt content. Those with low Co loadings (x = 0, 0.1, 0.3, and 0.5) display a completely diffusion controlling manner on account of their high Warburg resistance. In this context, the ionic diffusion is suppressed, resulting in a severe decline in the diffusion of ions from the electrolyte to the electrode surface. On the contrary, those with high Co concentrations (x = 0.7, 0.9, and 1.0) enjoy a low Warburg resistance, manifesting a more capacitive manner than the other samples. Consequently, the ion diffusion path is alleviated more efficiently, and capacitive current can be improved. It is worth noting that the $Co_{0.9}Ni_{0.1}$Ferrite showed the lowest Rct and Warburg resistance among the second group of samples, providing more efficacious capacitive current and therefore enhanced electrocatalytic activity.

Table 3. Calculated Values of the Equivalent Circuit Elements for the Samples

sample	Re (Ω)	CPE-T ($mFsp^{-1}$)	CPE-P	Rct (Ω)	W–R (Ω)
NiFerrite	12.5	8.6×10^{-6}	0.8	218	17365
$Co_{0.1}Ni_{0.9}$Ferrite	10.85	7.56×10^{-6}	0.86	191.3	9891
$Co_{0.3}Ni_{0.7}$Ferrite	12.14	1.23×10^{-6}	0.91	184.6	8617
$Co_{0.5}Ni_{0.5}$Ferrite	11.9	1.14×10^{-7}	0.78	172.9	35871
$Co_{0.7}Ni_{0.3}$Ferrite	13.17	7.74×10^{-5}	0.70	10391	410.2
$Co_{0.9}Ni_{0.1}$Ferrite	12.6	8.4×10^{-5}	0.83	7365	152.4
CoFerrite	12.1	3.8×10^{-5}	0.79	9538	161.7

3. CONCLUSIONS

In summary, Co_xNi_{1-x}Ferrite (x = 0.0, 0.1, 0.3, 0.5, 0.7 and 1.0) nanoparticles with varying compositions were successfully prepared using a microwave auto-combustion method. The adopted combustion approach is a facile, highly affordable, and readily adaptable route to synthesize non-polluting materials. The resultant products were manipulated as HER and OER electrocatalysts in a 1 M KOH medium. The electrochemical experiments proved that CoFerrite (422 mV at −10 mA cm^{-2}) and $Co_{0.9}Ni_{0.1}$Ferrite (419 mV at 10 mA cm^{-2}) possess the best electrocatalytic activities for HER and OER, separately. From the Tafel slope point of view, $Co_{0.9}Ni_{0.1}$Ferrite holds the smallest value for OER, 89.1 mV dec^{-1}, suggesting alleviated kinetics compared to other samples. The same behavior was observed for HER kinetics except that, $Co_{0.9}Ni_{0.1}$Ferrite has slower kinetics than CoFerrite (81.1 mV dec^{-1} vs 72.7 mV dec^{-1}). Our findings pave the path for developing green electrocatalysts by the virtue of highly economical precursors.

4. EXPERIMENTAL SECTION

4.1. Preparation of Catalysts. The reaction process was elaborated in our previous work.[48] In brief, for a normal synthesis procedure, $Fe(NO_3)_3.9H_2O$, $Ni(NO_3)_2.5H_2O$, and $Co(NO_3)_2.6H_2O$ were employed as metal sources, and NH_2CH_2COOH and NH_4NO_3 were utilized as the fuel and oxidizer, respectively. In order to prepare $Co_xNi_{1-x}Fe_2O_4$ (x = 0.0, 0.1, 0.3, 0.5, 0.7 and 1.0) nanoparticles, first $Fe(NO_3)_3 \cdot 9H_2O$ (2 mmol), $Co(NO_3)_2 \cdot 6H_2O$, and $Ni(NO_3)_2 \cdot 5H_2O$ with certain molar ratios, NH_2CH_2COOH (3 mmol), and NH_4NO_3(6 mmol) were mixed. The mixture was then transferred into an alumina crucible covered by a jacket layer of CuO to draw the microwave energy and generate calcination heat. For thermal treatment, the alumina crucible was placed in a domestic microwave oven with a power of 450 W for 30 min. The resulting powder was collected, washed several times with distilled water and ethanol to remove the residual initial materials, and dried in a hot air oven at 80 °C for 24 h. The final products were labeled as Co_xNi_{1-x}Ferrite (refer to Figure 9).

4.2. Apparatus and Procedure. *4.2.1. Apparatus.* To examine the structural aspects of the as-synthesized materials, a Rigaku Mini Flex 600; Cu Kα (λ = 1.5418 Å) XRD was used. XRD patterns were recorded in the 2θ ranging from 10 to 90°. A zero-background powder specimen holder was utilized for the XRD analysis of all samples. To identify the functional groups a JASCO 6800 FTIR FULL VACUUM & FTIR MICROSCOPE FT-IR apparatus was employed and the spectra were collected in the wavenumber region of 4000–400 cm^{-1} with the aid of the KBr pellet approach. Field emission scanning electron microscopy (FESEM) images were achieved on a TESCAN MIRA3 microscope, operated at 15 kV. In addition, EDS was carried out by Zeiss Ultra Plus FESEM at an accelerating voltage of 5 kV. Further examination on morphology was accomplished through TEM images, taken by a Hitachi HT7700 TEM instrument, functioning at the

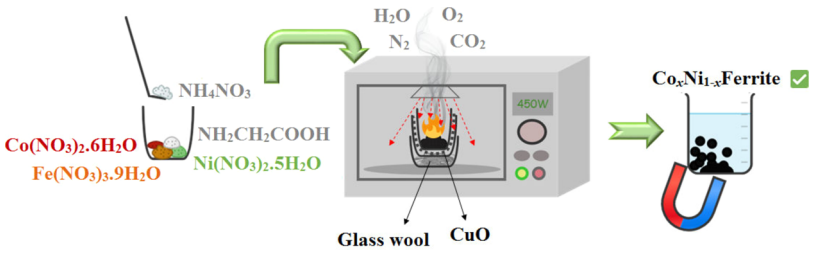


Figure 9. Schematic illustration of synthesis procedure.

https://doi.org/10.1021/acsomega.1c05183
ACS Omega 2021, 6, 33024–33032

accelerating voltage of 120 kV. The high-resolution transmission electron microscope images were obtained by the Thermo Scientific Talos F200S 200 kV TEM. The magnetic tests were implemented at ambient conditions employing a vibrating sample magnetometer, model VSM, LBKFB, with a maximum magnetic field of 10 kQe. Finally, to determine the BET specific surface area of the powder products, a Micromeritics ASAP 2010 instrument was exploited.

4.2.2. Electrode Fabrication. The catalysts inks were made by thoroughly mixing 1 mg of resulting powders in a 480 μL pure ethanol−deionized water mixture (380:100) under ultrasonication for 20 min, followed by the addition of 5% wt Nafion solution (5 μL) to the mentioned mixture, accompanied by another 20 min of ultrasonication. 10 μL of the homogeneous catalyst ink was pipetted out on the - fresh surface of cleaned glassy carbon (GC). Finally, the drying process of the catalyst-coated surface of the GC electrode was carried out in the presence of an air atmosphere at 80 °C for 120 min. To construct the working electrodes of reference commercial materials, 10% Pt/C and RuO_2, identical steps were followed. The loading amount of catalysts for each run was about ∼0.125 mg/cm^2.

4.2.3. Electrochemical Measurements. To evaluate the electrochemical characteristics of the prepared electrocatalysts, we followed a similar strategy to our earlier report 19. Succinctly, the electrochemical tests were performed on a VersaSTAT Potentiostat Galvanostat by means of a normal three-electrode cell containing reversible hydrogen electrode (RHE; HydroFlex) and Pt wire as reference and counter electrodes, respectively, under 1 M KOH medium. A 3 mm-diameter GC was employed as a working electrode, polished with = Al_2O_3 slurry (0.3 μm) and ultrasonically washed with distilled water and ethanol each for 10 min prior to each run. To this end, the LSV curves were recorded from 0 to −1.2 V and 0 to +1.8 V toward HER and OER, separately. The required overpotential for water reduction and oxidation were calculated at a current density of 10 mA cm^{-2}. Furthermore, a frequency ranged from 100 kHz and 0.1 Hz with a 10 mV RMS sinusoidal modulation at 0 V was considered to obtain the EIS curves.

■ ASSOCIATED CONTENT

Supporting Information

The Supporting Information is available free of charge at https://pubs.acs.org/doi/10.1021/acsomega.1c05183.

Data of SEM images, EDS elemental mappings, crystallite size table, table of the HER and OER performances of previous works, and SEM images and EDS graphs after electrochemical experiments (PDF)

■ AUTHOR INFORMATION

Corresponding Authors

Maasoumeh Khatamian − *Inorganic Chemistry Department, Faculty of Chemistry, University of Tabriz, Tabriz 5166616471, Iran*; Email: mkhatamian@yahoo.com

Umut Aydemir − *Koç University Boron and Advanced Materials Application and Research Center (KUBAM), Istanbul 34450, Turkey; Department of Chemistry, Koç University, Istanbul 34450, Turkey;* orcid.org/0000-0003-1164-1973; Email: uaydemir@ku.edu.tr

Authors

Sanaz Chamani − *Inorganic Chemistry Department, Faculty of Chemistry, University of Tabriz, Tabriz 5166616471, Iran*

Naeimeh Sadat Peighambardoust − *Koç University Boron and Advanced Materials Application and Research Center (KUBAM), Istanbul 34450, Turkey*

Complete contact information is available at: https://pubs.acs.org/10.1021/acsomega.1c05183

Author Contributions

S.C. synthesized and characterized the electrocatalysts. N.S.P. prepared the electrodes and conducted the electrochemical experiments. M.K. and U.A. supervised the whole project from synthesis to interpretation of the results. All authors contributed to the writing of the manuscript and approved its final version.

Notes

The authors declare no competing financial interest.

■ ACKNOWLEDGMENTS

U.A. acknowledges the funding support provided by the Turkish Academy of Sciences - Outstanding Young Scientist Award Program. M. KH. thanks the University of Tabriz and IRAN Nanotechnology Innovation Council (INIC) for their help and support. The authors would like to show their gratitude to Dr. Barış Yağcı and Dr. Amir Motallebzadeh from Koç University Surface Science and Technology Center (KUYTAM) as well as Zafer Eroğlu from Koç University for their help with chemical characterizations. We acknowledge Dr. Suleyman Tekmen from Bayburt University Central Research Laboratory (BUMER) for the HRTEM measurement.

■ REFERENCES

(1) Alshehri, S. M.; Alhabarah, A. N.; Ahmed, J.; Naushad, M.; Ahamad, T.; science, i. An efficient and cost-effective tri-functional electrocatalyst based on cobalt ferrite embedded nitrogen doped carbon. *J. Colloid Interface Sci.* **2018**, *514*, 1−9.

(2) Wang, S.; Bendt, G.; Saddeler, S.; Schulz, S. Synergistic Effects of Mo2C-NC@ CoxFey Core−Shell Nanoparticles in Electrocatalytic Overall Water Splitting Reaction. *Energy Technol.* **2019**, *7*, 1801121.

(3) Abbaspour, A.; Mirahmadi, E. Electrocatalytic hydrogen evolution reaction on carbon paste electrode modified with Ni ferrite nanoparticles. *Fuel* **2013**, *104*, 575−582.

(4) Zhao, X.; Yang, Z.; Wang, W.; Li, Y.; Zhou, X.; Zhang, H. Highly dispersed ultrafine shell-like nano-Pt with efficient hydrogen evolution via metal boron organic polymers. *J. Mater. Chem. A* **2020**, *8*, 7171−7176.

(5) Yuan, F.; Cheng, X.; Wang, M.; Ni, Y. Controlled synthesis of tubular ferrite MFe2O4 (M= Fe, Co, Ni) microstructures with efficiently electrocatalytic activity for water splitting. *Electrochim. Acta* **2019**, *324*, 134883.

(6) Yang, Y.; Fei, H.; Ruan, G.; Tour, J. M. Porous cobalt-based thin film as a bifunctional catalyst for hydrogen generation and oxygen generation. *Adv. Mater.* **2015**, *27*, 3175−3180.

(7) Liu, J.; Zhao, S.; Wang, C.; Ma, Y.; He, L.; Liu, B.; Zhang, Z. Catkin-derived mesoporous carbon-supported molybdenum disulfide and nickel hydroxyl oxide hybrid as a bifunctional electrocatalyst for driving overall water splitting. *J. Colloid Interface Sci.* **2022**, *608*, 1627−1637.

(8) Septiani, N. L. W.; Kaneti, Y. V.; Fathoni, K. B.; Kani, K.; Allah, A. E.; Yuliarto, B.; Nugraha; Dipojono, H. K.; Alothman, Z. A.; Golberg, D.; Yamauchi, Y. Self-assembly of two-dimensional bimetallic nickel−cobalt phosphate nanoplates into one-dimensional

porous chainlike architecture for efficient oxygen evolution reaction. *Chem. Mater.* **2020**, *32*, 7005−7018.
(9) Debnath, B.; Parvin, S.; Dixit, H.; Bhattacharyya, S. Oxygen-Defect-Rich Cobalt Ferrite Nanoparticles for Practical Water Electrolysis with High Activity and Durability. *ChemSusChem* **2020**, *13*, 3875−3886.
(10) Jian, J.; Chen, W.; Zeng, D.; Chang, L.; Zhang, R.; Jiang, M.; Yu, G.; Huang, X.; Yuan, H.; Feng, S. Metal-ionic-conductor potassium ferrite nanocrystals with intrinsic superhydrophilic surfaces for electrocatalytic water splitting at ultrahigh current densities. *J. Mater. Chem. A* **2021**, *9*, 7586−7593.
(11) Liu, J.; Zhu, D.; Ling, T.; Vasileff, A.; Qiao, S.-Z. S-NiFe2O4 ultra-small nanoparticle built nanosheets for efficient water splitting in alkaline and neutral pH. *Nano Energy* **2017**, *40*, 264−273.
(12) Wang, X.; Su, R.; Aslan, H.; Kibsgaard, J.; Wendt, S.; Meng, L.; Dong, M.; Huang, Y.; Besenbacher, F. Tweaking the composition of NiMoZn alloy electrocatalyst for enhanced hydrogen evolution reaction performance. *Nano Energy* **2015**, *12*, 9−18.
(13) Yang, Y.; Lin, Z.; Gao, S.; Su, J.; Lun, Z.; Xia, G.; Chen, J.; Zhang, R.; Chen, Q. Tuning electronic structures of nonprecious ternary alloys encapsulated in graphene layers for optimizing overall water splitting activity. *ACS Catal.* **2017**, *7*, 469−479.
(14) Zeng, M.; Chen, Y.; Li, J.; Xue, H.; Mendes, R. G.; Liu, J.; Zhang, T.; Rümmeli, M. H.; Fu, L. 2D WC single crystal embedded in graphene for enhancing hydrogen evolution reaction. *Nano Energy* **2017**, *33*, 356−362.
(15) Zhu, J.; Sakaushi, K.; Clavel, G.; Shalom, M.; Antonietti, M.; Fellinger, T.-P. A general salt-templating method to fabricate vertically aligned graphitic carbon nanosheets and their metal carbide hybrids for superior lithium ion batteries and water splitting. *J. Am. Chem. Soc.* **2015**, *137*, 5480−5485.
(16) Zhang, B.; Xiao, C.; Xie, S.; Liang, J.; Chen, X.; Tang, Y. Iron−nickel nitride nanostructures in situ grown on surface-redox-etching nickel foam: efficient and ultrasustainable electrocatalysts for overall water splitting. *Chem. Mater.* **2016**, *28*, 6934−6941.
(17) Wang, Y.; Liu, D.; Liu, Z.; Xie, C.; Huo, J.; Wang, S. Porous cobalt−iron nitride nanowires as excellent bifunctional electrocatalysts for overall water splitting. *Chem. Commun.* **2016**, *52*, 12614−12617.
(18) Ou, G.; Fan, P.; Zhang, H.; Huang, K.; Yang, C.; Yu, W.; Wei, H.; Zhong, M.; Wu, H.; Li, Y. Large-scale hierarchical oxide nanostructures for high-performance electrocatalytic water splitting. *Nano Energy* **2017**, *35*, 207−214.
(19) Gao, X.; Zhang, H.; Li, Q.; Yu, X.; Hong, Z.; Zhang, X.; Liang, C.; Lin, Z. Hierarchical NiCo2O4 hollow microcuboids as bifunctional electrocatalysts for overall water-splitting. *Angew. Chem., Int. Ed.* **2016**, *55*, 6290−6294.
(20) Peighambardoust, N. S.; Khameneh Asl, S.; Maghsoudi, M. The effect of doping concentration of TiO2 nanotubes on energy levels and its direct correlation with photocatalytic activity. *Thin Solid Films* **2019**, *690*, 137558.
(21) Ha, D.-H.; Han, B.; Risch, M.; Giordano, L.; Yao, K. P. C.; Karayaylali, P.; Shao-Horn, Y. Activity and stability of cobalt phosphides for hydrogen evolution upon water splitting. *Nano Energy* **2016**, *29*, 37−45.
(22) Huang, Z.; Chen, Z.; Chen, Z.; Lv, C.; Humphrey, M. G.; Zhang, C. Cobalt phosphide nanorods as an efficient electrocatalyst for the hydrogen evolution reaction. *Nano Energy* **2014**, *9*, 373−382.
(23) Septiani, N. L. W.; Kaneti, Y. V.; Fathoni, K. B.; Guo, Y.; Ide, Y.; Yuliarto, B.; Jiang, X.; Nugraha, H. K.; Dipojono, H. K.; Golberg, D.; Yamauchi, Y. Tailorable nanoarchitecturing of bimetallic nickel−cobalt hydrogen phosphate via the self-weaving of nanotubes for efficient oxygen evolution. *J. Mater. Chem. A* **2020**, *8*, 3035−3047.
(24) Mete, B.; Peighambardoust, N. S.; Aydin, S.; Sadeghi, E.; Aydemir, U. J. E. A. Metal-Substituted Zirconium Diboride (Zr1-xTMxB2; TM= Ni, Co, and Fe) as Low-Cost and High-Performance Bifunctional Electrocatalyst for Water Splitting. *Electrochim. Acta* **2021**, *389*, 138789.
(25) Chen, Z.; Duan, X.; Wei, W.; Wang, S.; Zhang, Z.; Ni, B.-J. Boride-based electrocatalysts: Emerging candidates for water splitting. *Nano Res.* **2020**, *13*, 293−314.
(26) Konkena, B.; Masa, J.; Xia, W.; Muhler, M.; Schuhmann, W. MoSSe@ reduced graphene oxide nanocomposite heterostructures as efficient and stable electrocatalysts for the hydrogen evolution reaction. *Nano Energy* **2016**, *29*, 46−53.
(27) Gao, M.-R.; Liang, J.-X.; Zheng, Y.-R.; Xu, Y.-F.; Jiang, J.; Gao, Q.; Li, J.; Yu, S.-H. An efficient molybdenum disulfide/cobalt diselenide hybrid catalyst for electrochemical hydrogen generation. *Nat. Commun.* **2015**, *6*, 5982.
(28) Cao, L.; Li, Z.; Su, K.; Zhang, M.; Cheng, B. Rational design of hollow oxygen deficiency-enriched NiFe2O4@ N/rGO as bifunctional electrocatalysts for overall water splitting. *J. Energy Chem.* **2021**, *54*, 595−603.
(29) Navadeepthy, D.; Rebekah, A.; Viswanthan, C.; Ponpandian, N. Boosting the kinetics of oxygen and hydrogen evolution in alkaline water splitting using nickel ferrite/N-graphene nanocomposite as a bifunctional electrocatalyst. *Int. J. Hydrogen Energy* **2021**, *46*, 21512−21524.
(30) Zhang, C.; Bhoyate, S.; Zhao, C.; Kahol, P.; Kostoglou, N.; Mitterer, C.; Hinder, S.; Baker, M.; Constantinides, G.; Polychronopoulou, K.; Rebholz, C.; Gupta, R. Electrodeposited nanostructured CoFe2O4 for overall water splitting and supercapacitor applications. *Catalysts* **2019**, *9*, 176.
(31) Hu, H.; Guan, B.; Xia, B.; Lou, X. W. Designed formation of Co3O4/NiCo2O4 double-shelled nanocages with enhanced pseudocapacitive and electrocatalytic properties. *J. Am. Chem. Soc.* **2015**, *137*, 5590−5595.
(32) Fu, W.; Zhao, C.; Han, W.; Liu, Y.; Zhao, H.; Ma, Y.; Xie, E. Cobalt sulfide nanosheets coated on NiCo 2 S 4 nanotube arrays as electrode materials for high-performance supercapacitors. *J. Mater. Chem. A* **2015**, *3*, 10492−10497.
(33) Chauhan, M.; Reddy, K. P.; Gopinath, C. S.; Deka, S. Copper cobalt sulfide nanosheets realizing a promising electrocatalytic oxygen evolution reaction. *ACS Catal.* **2017**, *7*, 5871−5879.
(34) Chakrapani, K.; Bendt, G.; Hajiyani, H.; Schwarzrock, I.; Lunkenbein, T.; Salamon, S.; Landers, J.; Wende, H.; Schlögl, R.; Pentcheva, R.; Behrens, M.; Schulz, S. Role of composition and size of cobalt ferrite nanocrystals in the oxygen evolution reaction. *ChemCatChem* **2017**, *9*, 2988−2995.
(35) Sahoo, P.; Tan, J.-B.; Zhang, Z.-M.; Singh, S. K.; Lu, T.-B. Engineering the Surface Structure of Binary/Ternary Ferrite Nanoparticles as High-Performance Electrocatalysts for the Oxygen Evolution Reaction. *ChemCatChem* **2018**, *10*, 1075−1083.
(36) Liu, Y.; Bai, Y.; Han, Y.; Yu, Z.; Zhang, S.; Wang, G.; Wei, J.; Wu, Q.; Sun, K. Self-supported hierarchical FeCoNi-LTH/NiCo2O4/CC electrodes with enhanced bifunctional performance for efficient overall water splitting. *ACS Appl. Mater. Interfaces* **2017**, *9*, 36917−36926.
(37) Yin, J.; Zhou, P.; An, L.; Huang, L.; Shao, C.; Wang, J.; Liu, H.; Xi, P. Self-supported nanoporous NiCo 2 O 4 nanowires with cobalt−nickel layered oxide nanosheets for overall water splitting. *Nanoscale* **2016**, *8*, 1390−1400.
(38) Wu, Z.; Wang, X.; Huang, J.; Gao, F. A Co-doped Ni−Fe mixed oxide mesoporous nanosheet array with low overpotential and high stability towards overall water splitting. *J. Mater. Chem. A* **2018**, *6*, 167−178.
(39) Osgood, H.; Devaguptapu, S. V.; Xu, H.; Cho, J.; Wu, G. Transition metal (Fe, Co, Ni, and Mn) oxides for oxygen reduction and evolution bifunctional catalysts in alkaline media. *Nano Today* **2016**, *11*, 601−625.
(40) Dhas, C. R.; Monica, S.; Jothivenkatachalam, K.; Nathanael, A. J.; Kavinkumar, V.; Venkatesh, R.; Arivukarasan, D. Direct-grown nebulizer-sprayed nickel-copper mixed metal oxide nanocomposite films as bifunctional electrocatalyst for water splitting. *Ionics* **2021**, 1−14.
(41) Naseri, M. G.; Saion, E. B.; Ahangar, H. A.; Hashim, M.; Shaari, A. H. Simple preparation and characterization of nickel ferrite

https://doi.org/10.1021/acsomega.1c05183
ACS Omega 2021, 6, 33024−33032

nanocrystals by a thermal treatment method. *Powder Technol.* **2011**, *212*, 80−88.
(42) Zi, Z.; Sun, Y.; Zhu, X.; Yang, Z.; Dai, J.; Song, W. Synthesis and magnetic properties of CoFe2O4 ferrite nanoparticles. *J. Magn. Magn. Mater.* **2009**, *321*, 1251−1255.
(43) Mallesh, S.; Srinivas, V.; Vasundhara, M.; Kim, K. H. Low-temperature magnetization behaviors of superparamagnetic MnZn ferrites nanoparticles. *Phys. B* **2020**, *582*, 411963.
(44) Padmapriya, G.; Manikandan, A.; Krishnasamy, V.; Jaganathan, S. K.; Antony, S. A. Spinel NixZn1− xFe2O4 (0.0≤ x≤ 1.0) nano-photocatalysts: synthesis, characterization and photocatalytic degradation of methylene blue dye. *J. Mol. Struct.* **2016**, *1119*, 39−47.
(45) Sertkol, M.; Köseoğlu, Y.; Baykal, A.; Kavas, H.; Bozkurt, A.; Toprak, M. S. Microwave synthesis and characterization of Zn-doped nickel ferrite nanoparticles. *J. Alloys Compd.* **2009**, *486*, 325−329.
(46) Mahmoud, M. H.; Elshahawy, A. M.; Makhlouf, S. A.; Hamdeh, H. H. Mössbauer and magnetization studies of nickel ferrite nanoparticles synthesized by the microwave-combustion method. *J. Magn. Magn. Mater.* **2013**, *343*, 21−26.
(47) Kombaiah, K.; Vijaya, J. J.; Kennedy, L. J.; Bououdina, M.; Al-Najar, B. Conventional and microwave combustion synthesis of optomagnetic CuFe2O4 nanoparticles for hyperthermia studies. *J. Phys. Chem. Solids* **2018**, *115*, 162−171.
(48) Dehghani, M.; Tadjarodi, A.; Chamani, S. Synthesis and Characterization of Magnetic Zeolite Y−Palladium−Nickel Ferrite by Ultrasonic Irradiation and Investigating Its Catalytic Activity in Suzuki−Miyaura Cross-Coupling Reactions. *ACS Omega* **2019**, *4*, 10640−10648.
(49) Zhang, G.; Zheng, X.; Xu, Q.; Zhang, J.; Liu, W.; Chen, J. Carbon nanotube-induced phase and stability engineering: a strained cobalt-doped WSe 2/MWNT heterostructure for enhanced hydrogen evolution reaction. *J. Mater. Chem. A* **2018**, *6*, 4793−4800.
(50) Wang, J.; Liao, T.; Wei, Z.; Sun, J.; Guo, J.; Sun, Z. Heteroatom-Doping of Non-Noble Metal-Based Catalysts for Electrocatalytic Hydrogen Evolution: An Electronic Structure Tuning Strategy. *Small Methods* **2021**, *5*, 2000988.
(51) Xiong, Q.; Zhang, X.; Wang, H.; Liu, G.; Wang, G.; Zhang, H.; Zhao, H. One-step synthesis of cobalt-doped MoS 2 nanosheets as bifunctional electrocatalysts for overall water splitting under both acidic and alkaline conditions. *Chem. Commun.* **2018**, *54*, 3859−3862.
(52) Wang, D.-Y.; Gong, M.; Chou, H.-L.; Pan, C.-J.; Chen, H.-A.; Wu, Y.; Lin, M.-C.; Guan, M.; Yang, J.; Chen, C.-W.; Wang, Y.-L.; Hwang, B.-J.; Chen, C.-C.; Dai, H. Highly active and stable hybrid catalyst of cobalt-doped FeS2 nanosheets−carbon nanotubes for hydrogen evolution reaction. *J. Am. Chem. Soc.* **2015**, *137*, 1587−1592.
(53) Loni, E.; Shokuhfar, A.; Siadati, M. H. Cobalt-Based Electrocatalysts for Water Splitting: An Overview. *Catal. Surv. Asia* **2021**, *25*, 114−147.
(54) Wang, X.; Huang, X.; Gao, W.; Tang, Y.; Jiang, P.; Lan, K.; Yang, R.; Wang, B.; Li, R. Metal−organic framework derived CoTe 2 encapsulated in nitrogen-doped carbon nanotube frameworks: a high-efficiency bifunctional electrocatalyst for overall water splitting. *J. Mater. Chem. A* **2018**, *6*, 3684−3691.
(55) Gao, J.; Liu, L.; Qiu, H.-J.; Wang, Y. Engineering phase transformation of cobalt selenide in carbon cages and the phases' bifunctional electrocatalytic activity for water splitting. *Nanotechnology* **2017**, *28*, 315401.
(56) Fan, H. J.; Gösele, U.; Zacharias, M. Formation of nanotubes and hollow nanoparticles based on Kirkendall and diffusion processes: a review. *Small* **2007**, *3*, 1660−1671.
(57) Kumbhar, V. S.; Jagadale, A. D.; Shinde, N. M.; Lokhande, C. D. Chemical synthesis of spinel cobalt ferrite (CoFe2O4) nano-flakes for supercapacitor application. *Appl. Surf. Sci.* **2012**, *259*, 39−43.
(58) Hu, C.; Zhang, L.; Zhao, Z.-J.; Li, A.; Chang, X.; Gong, J. Synergism of geometric construction and electronic regulation: 3D Se-(NiCo) Sx/(OH) x nanosheets for highly efficient overall water splitting. *Adv. Mater.* **2018**, *30*, 1705538.
(59) Zhang, H.; Qian, G.; Chen, X.; Jiang, W.; Yu, T.; Wang, Y.; Luo, L.; Yin, S. Engineering, V2O3-decorated spinel CoFe2O4 with carbon-encapsulated mesoporous nanosheets for efficient water splitting. *ACS Sustainable Chem. Eng.* **2021**, *9*, 980−986.
(60) Li, T.; Lv, Y.; Su, J.; Wang, Y.; Yang, Q.; Zhang, Y.; Zhou, J.; Xu, L.; Sun, D.; Tang, Y. Anchoring CoFe2O4 nanoparticles on N-doped carbon nanofibers for high-performance oxygen evolution reaction. *Adv. Sci.* **2017**, *4*, 1700226.
(61) Kargar, A.; Yavuz, S.; Kim, T. K.; Liu, C.-H.; Kuru, C.; Rustomji, C. S.; Jin, S.; Bandaru, P. R. Solution-processed CoFe2O4 nanoparticles on 3D carbon fiber papers for durable oxygen evolution reaction. *ACS Appl. Mater. Interfaces* **2015**, *7*, 17851−17856.
(62) Li, S.; Sirisomboonchai, S.; Yoshida, A.; An, X.; Hao, X.; Abudula, A.; Guan, G. Bifunctional CoNi/CoFe 2 O 4/Ni foam electrodes for efficient overall water splitting at a high current density. *J. Mater. Chem. A* **2018**, *6*, 19221−19230.
(63) Jin, H.; Wang, J.; Su, D.; Wei, Z.; Pang, Z.; Wang, Y. In situ cobalt−cobalt oxide/N-doped carbon hybrids as superior bifunctional electrocatalysts for hydrogen and oxygen evolution. *J. Am. Chem. Soc.* **2015**, *137*, 2688−2694.
(64) Li, P.; Ma, R.; Zhou, Y.; Chen, Y.; Zhou, Z.; Liu, G.; Liu, Q.; Peng, G.; Liang, Z.; Wang, J. In situ growth of spinel CoFe 2 O 4 nanoparticles on rod-like ordered mesoporous carbon for bifunctional electrocatalysis of both oxygen reduction and oxygen evolution. *J. Mater. Chem. A* **2015**, *3*, 15598−15606.
(65) Feng, Y.; Li, Y.; Hou, F. Preparation and electrochemical properties of Cr doped LiV3O8 cathode for lithium ion batteries. *Mater. Lett.* **2009**, *63*, 1338−1340.
(66) Masa, J.; Barwe, S.; Andronescu, C.; Sinev, I.; Ruff, A.; Jayaramulu, K.; Elumeeva, K.; Konkena, B.; Roldan Cuenya, B.; Schuhmann, W. Low overpotential water splitting using cobalt−cobalt phosphide nanoparticles supported on nickel foam. *ACS Energy Lett.* **2016**, *1*, 1192−1198.
(67) Sadeghi, E.; Peighambardoust, N. S.; Khatamian, M.; Unal, U.; Aydemir, U. Metal doped layered MgB 2 nanoparticles as novel electrocatalysts for water splitting. *Sci. Rep.* **2021**, *11*, 3337.
(68) Kuang, P.; Tong, T.; Fan, K.; Yu, J. In situ fabrication of Ni−Mo bimetal sulfide hybrid as an efficient electrocatalyst for hydrogen evolution over a wide pH range. *ACS Catal.* **2017**, *7*, 6179−6187.
(69) Zheng, Y.; Jiao, Y.; Zhu, Y.; Li, L. H.; Han, Y.; Chen, Y.; Du, A.; Jaroniec, M.; Qiao, S. Z. J. N. c. Hydrogen evolution by a metal-free electrocatalyst. *Nat. Commun.* **2014**, *5*, 3783.
(70) Laursen, A. B.; Kegnæs, S.; Dahl, S.; Chorkendorff, I. Molybdenum sulfides—efficient and viable materials for electro-and photoelectrocatalytic hydrogen evolution. *Energy Environ. Sci.* **2012**, *5*, 5577−5591.

https://doi.org/10.1021/acsomega.1c05183
ACS Omega 2021, 6, 33024−33032